Hindawi
Advances in Materials Science and Engineering
Volume 2022, Article ID 9259324, 12 pages
https://doi.org/10.1155/2022/9259324

Research Article

Local and Global Interactive Buckling Capacity of Thin-Walled Box-Section Members of BS700 High-Strength Steel under Axial Compression

Gao Lei, Ni ming, Xie Xingkun, Bai Linyue, and He Lixiang

College of Field Engineering and Army Engineering University of PLA, Nanjing 210007, China

Correspondence should be addressed to Xie Xingkun; jfxie2020@sina.com

Received 16 July 2021; Accepted 21 March 2022; Published 7 July 2022

Academic Editor: Antonio Caggiano

The local and global buckling capacity of the thin-walled box-section members formed by cold bending of ten BS700 high-strength steel (HSS) specimens are experimentally determined through an axial compression test. The mechanical properties of the materials are evaluated through material performance test, and a material model suitable for finite element analysis is proposed. The initial geometric imperfection of the members is measured, and it is found that the maximum initial deflection can be 1/1000 of the length of the members, as specified in the Chinese code. Based on the test, the ultimate bearing capacity and failure modes of the component with local and global interactive buckling are obtained. Further, a finite element model is established, and the corresponding results are compared with the test results. Furthermore, the test results are compared with those obtained using the existing specifications. The results show that the failure modes of the specimens are primarily local and global buckling failure. The influence of residual stress and initial geometric imperfection is considered in the proposed finite element model. Comparing the ultimate bearing capacity and load-displacement curves with the corresponding test results, it is found that the finite element model can effectively reproduce the test results. By comparing the test results with those obtained based on the steel structure design codes of China, the United States, and Europe, it is found that the test results are all higher than the existing code results, and the Chinese and European codes are relatively conservative with a difference of more than 20%, while the difference between the test results and the American code results is nearly 10%. Therefore, it is necessary to further improve the calculation methods of local and global buckling capacity of thin-walled box-section members of BS700 HSS under axial compression.

1. Introduction

The use of high-strength steel (HSS) materials in construction and bridge engineering can reduce the section size and structural dead weight of components, leading to several advantages such as reduction in the welding seam size and welding workload, decrease in the cost of processing, transportation, construction, and installation of structural components, and creation of a large building usage space [1–4]. Therefore, HSS has always received significant attention in the construction and structural industries. The pillars of the Star City Hotel in Sydney, Australia, are made of S690 HSS. The Landmark Tower in Yokohama and some tall buildings in Shimizu, Japan, have used steel with a yield strength of 600 MPa. S460 and S690 steel roof trusses were used in some buildings in Berlin, Germany, and S460 steel was used in the Rhine Bridge. High-performance steel bridges have been demonstrated in Tennessee and Nebraska in the United States, which promoted the application of HSS for bridge construction in the United States. Sweden's 48 m fast military bridge was built with ultra HSS (S960 and S1100), which effectively reduced the bridge's dead weight [5–8].

China used Q460 HSS in 2008 for the main structure of the "Bird's Nest" national stadium [9]. Subsequently, the new building of CCTV [10] and Pudong Financial Square [11] also adopted Q460 steel. Over the recent years, steel products with yield strengths of 500, 590, 620, and 690 MPa have been gradually recommended in building structures [9]. Some removable bridge structures for an emergency purpose have used heat-treated HSS with nominal yield

strength up to 700 MPa or higher [12, 13]. With the rapid development of the global economy, higher-strength steel is expected to be increasingly utilized in the construction and bridge industries.

The stability of HSS members has been extensively investigated over recent years. In addition to the global buckling and local buckling of HSS, the local and global interactive buckling has received considerable research attention. Local buckling and global buckling are always closely related to each other because the global buckling of thin-walled members of HSS cannot be completely separated from the local buckling of the plate. Little et al. [14] proposed a yield strength reduction method (effective yield strength method) for determining the local and global buckling capacity of welded thin-walled box-section compression rods, which was adopted by the US specification for structural steel buildings [15]. Schafer et al. [16, 17] proposed a direct strength method to calculate the ultimate bearing capacity of the plate after buckling for the axial compression members. Hancock et al. [18] used the finite strip method to calculate the local-global buckling capacity of I-section and box-section members under axial compression. Usami et al. [19, 20] experimentally studied the local and global interactive buckling of box-section members with a yield strength of 690 MPa and 460 MPa, and they proposed introducing the yield strength correction factor Q into the Perry formula to calculate the local and global interactive buckling. Based on a large number of experimental data, Winter et al. [21] proposed a practical calculation formula for the effective width method, which was adopted by the European specification [22] and Chinese specification [23]. Shanmugam et al. [24] examined the local and global buckling of the column using a method that comprehensively considered the effective width method, tangential stiffness method, and nonlinear numerical analysis. Degée et al. [25] studied the local and global interactive buckling of HSS welded box-section compression bars and proposed a calculation formula based on the effective width method.

Lin [26] used experimental tests and finite element analysis to obtain the global and local buckling of 390 MPa steel welded thin-walled box cross-section axial compression column. Furthermore, they compared the results with the relevant specifications and proposed suggestions on the use of specifications. Shen et al. [27] used numerical methods to analyze high-strength welded box-section axial compression members with excess width/thickness ratio and proposed a modified direct strength method. Chen et al. [28] examined the buckling capacity of thin-walled pressure rods with a width/thickness ratio exceeding the limit and proposed the relevant buckling calculation formulas for welded square and rectangular box-section axial compression members. Shu et al. [29] conducted stability axial compression tests on 10 Q550 HSS welded box-section members. Liu [30] used finite element software to analyze the local and global interactive buckling of the Q460 HSS welded box-section pressure bar. Cao [31] designed three different types of columns to investigate the study method for buckling behaviour of welded H-section columns fabricated from 800 MPa HSS. They examined different buckling behaviours, including the load-axial displacement curves, relationship between the local out-of-plane displacement and global overall lateral displacement, and ultimate load of the columns. Meanwhile, the effects of several parameters (the slenderness ratio, width-thickness ratio of the flange, and height-thickness ratio of the web) on the buckling behavior were investigated. According to the above literature survey, the local and global interactive buckling of the axial compression members has been primarily studied through experimental tests, numerical analysis, and some theoretical methods. Several formulas have been established to calculate the local and global buckling capacity of different steel columns. Meanwhile, the principal calculation methods of local and global buckling capacity are the yield strength reduction method and the effective width method. To prevent local buckling, many codes strictly restrict the width-thickness ratio of plates. Thus, the conclusions of the studies on local and global interactive buckling of HSS members are not consistent. The effective width method, yield strength reduction method, and direct strength method are suitable for different HSS members. However, the method suitable for BS700 HSS groove butt welding box-section members has not been established yet. Therefore, relevant tests and theoretical research are still needed to determine whether the current design specifications for steel structures are applicable to BS700 HSS members.

In this paper, the stability properties of thin-walled box-section columns formed by cold bending of ten BS700 HSS columns (with a nominal yield strength of 700 MPa) are investigated. Further, a finite element model is established to numerically simulate the test process. Furthermore, according to the difference between the test results and the data obtained by Chinese, American, and European design specifications for steel structures, the feasibility and applicability of the existing codes to determine the local and global interactive buckling capacity of thin-walled box-section members of BS700 HSS under axial compression are examined.

2. Test Conditions

2.1. Specimen Design. Ten specimens of thin-walled box-section members were made of BS700 HSS. Typically, the welding of HSS members is difficult. Therefore, to reduce the welding seam, the plate was cold-bent into a groove section during processing, and then, the thin-walled box section was formed by butt welding, which reduced two welds compared with those appearing in the general four plate welding. Carbon dioxide shielded arc welding was used as the welding method, and the gas flow was 18–20 L/min. DC reverse connection was used, where the electric current was 90–120 A and the voltage was 21–30 V. As shown in Figure 1, to simulate the boundary conditions of hinge at both ends as far as possible, a one-way hinge is installed at both upper and lower ends of the member, which also controls the instability of the specimen along the weak axis.

To ensure that the specimen is connected to the one-way hinge, a 15 mm thick steel plate is welded at the end of the specimen and bolted to the plate in the one-way hinge. To monitor the vertical displacement of the column, two

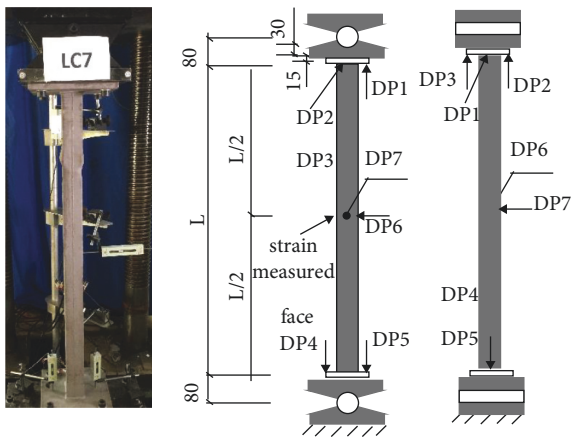

(a) (b)

Figure 1: Test loading device. (a) Field loading; (b) schematic of loading device.

displacement meters (DP2 and DP3) are used. Three displacement meters (DP1, DP4, and DP5) are utilized to monitor the vertical displacement. The DP6 displacement meter can monitor the lateral displacement and hinge rotation. The DP7 strain gauge measures the strain on the surface when buckling takes place. The distance between the rotation center of the one-way hinge and the end of the specimen is 80 mm, so the calculated hinge length (L) of the specimen is its original geometric length L_0 plus 160 mm, as shown in Table 1. Here, t, H, and B denote the thickness, section height, and section width of the column, respectively. To examine the influence of local buckling on global buckling, the two different sections (square and rectangular sections) are designed.

2.2. Measurement of Initial Geometric Imperfection of Specimens. A ruler and feeler were used to measure the initial geometric imperfection of the specimens as shown in Figure 2. The initial imperfection in the buckling plane along the weak axis was measured, and the front and rear planes were assessed. Two centerlines were taken from the edge and the middle of each plane. Three points at the end and the middle points on each line were considered as the measurement points, and then, the maximum value among all the measurement results was taken as the initial geometric imperfection.

The measurement results are shown in Table 2, where δ is the measured initial defect value, and δ/L is the ratio of the defect to the geometric length of the specimen.

It is clear from Table 2 that the ratio of global geometric imperfection to length is nearly 1/1000, indicating that the standard defect value of 1/1000 bar length stipulated in the existing specification can be adopted.

3. Test Results and Analysis

3.1. Material Performance Test Results. To evaluate the mechanical properties of BS700 HSS, three standard specimens were tested. The sample was obtained from the base material of the processed BS700 HSS groove butt welding box-section members according to the requirements of the Chinese standard "Sampling location and Sample Preparation for Mechanical Properties test of Steel and Steel Products" (GB/T 2975–2018) [31]. A strain gauge was pasted in the middle of the specimen, and it was loaded step by step on the tensile testing machine. The specific test result is shown in Figure 3. Here, x axis represents loading time (unit: s) and the y axis represents load (unit: kN).

When the material is damaged, there is a certain necking phenomenon if the fracture line is close to the horizontal line, indicating that the material has a good plastic property. Figure 4 shows a snapshot of the damaged material.

The elastic modulus and yield strength of BS700 HSS were determined through a material performance test. The elastic modulus was obtained by taking the slope of the linear

Table 1: Measured dimensions of specimens.

Specimen	t (mm)	L_0 (mm)	H (mm)	B (mm)	L (mm)
ts1	3.14	280.5		20.05	
ts2	3.12	281.2		20.00	
ts3	3.24	282.1		20.10	
LC1	2.98	996.3	106.3	105.9	1156.3
LC2	3.02	1398.4	105.8	105.7	1558.4
LC3	2.96	1798.5	104.2	106.8	1958.5
LC4	3.22	2198.2	106.4	106.1	2358.2
LC5	3.24	2600.5	106.5	105.3	2760.5
LC6	2.92	1097.5	105.7	75.6	1257.5
LC7	3.08	1398.6	105.4	75.7	1558.6
LC8	3.12	1597.4	104.3	75.1	1757.4
LC9	3.16	2199.7	105.7	75.5	2359.7
LC10	3.24	2796.6	106.1	75.4	2956.6

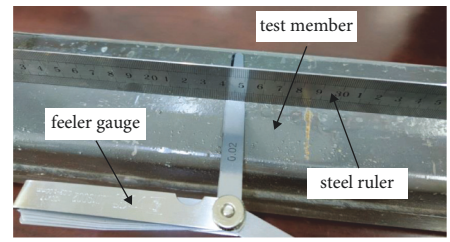

Figure 2: Measurement method of the initial geometric imperfection of specimens.

Table 2: Geometric initial imperfection along the weak axis direction.

Specimen	L (mm)	δ (mm)	δ/L
LC1	996.3	1.05	1/949
LC2	1398.4	1.57	1/891
LC3	1798.5	1.76	1/1022
LC4	2198.2	1.47	1/1495
LC5	2600.5	1.90	1/1369
LC6	897.5	0.75	1/1197
LC7	1298.6	1.30	1/999
LC8	1597.4	2.10	1/761
LC9	2199.7	1.90	1/1158
LC10	2796.6	2.70	1/1036

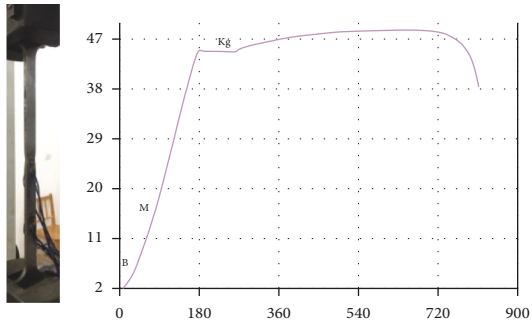

Figure 3: Mechanical property test of materials.

Figure 4: Image of a damaged specimen.

Table 3: Tension coupon test results.

Specimen	t (mm)	E (GPa)	f_y (MPa)	f_u (MPa)	f_y/f_u
ts1	3.14	192.7	738.2	790.2	0.9342
ts2	3.12	208.2	753.1	809.3	0.9306
ts3	3.24	205.6	748.7	798.9	0.9372
Average	3.17	202.2	746.7	799.5	0.9340

part of the stress-strain curve of the material. The results of the material performance test for the three specimens are shown in Table 3. Here, t, E, F_y, F_u, and F_y/F_u represent the plate thickness, elastic modulus, nominal yield strength, ultimate tensile strength, and the ratio of yield strength to tensile strength, respectively.

To better simulate the test data using the finite element method, the material curves used in the simulation were obtained by averaging three measured stress-strain curves. Further, the experimentally obtained stress and strain were actually the nominal stress and nominal strain, so they were transformed into real stress and strain by using finite element software ANSYS as follows:

$$\begin{aligned} \sigma &= \sigma_{\text{nom}}\left(1+\varepsilon_{\text{nom}}\right) \\ \varepsilon &= \ln\left(1+\varepsilon_{\text{nom}}\right), \end{aligned} \tag{1}$$

where ε is the real strain, σ is the real stress, σ_{nom} is the nominal stress, and ε_{nom} is the nominal strain. Three data points are needed in the follow-up multilinear strengthening model (trilinear model is considered in this report). The three points obtained after conversion according to the average value of the material test curves are as follows:

Yield point: $\sigma_s = 749.4$ MPa, and $\varepsilon_s = 0.0037$, where σ_s is the yield strength and ε_s is the yield strain.

Endpoints of yield stage: $\sigma_{se} = 754.1$MPa, and $\varepsilon_{se} = 0.0099\varepsilon_{se} = 0.0099$, where σ_{se} is the yield strength at the end of the yield stage and ε_{se} is the yield strain at the end of the yield stage.

Ultimate strength point: $\sigma_b = 818.1$ MPa, and $\varepsilon_b = 0.0233$, where σ_b is the ultimate strength and ε_b is the ultimate strain.

A comparison between the stress-strain curve obtained by the finite element method and the three measured stress-strain curves is shown in Figure 5. It is clear that the follow-up multilinear strengthening model can well simulate the stress-strain curve of the actual material.

4. Buckling Mode Analysis

As shown in Figure 6, the failure modes of the specimen are mainly local and global interactive buckling failure, and the column presents global buckling while the component plate of the column takes shows a local bulge. During the initial loading stage, both the vertical and lateral deformations of the specimen are very small. With the gradual increase of the load, the local buckling of the plate occurs, and the vertical deformation becomes larger. Subsequently, with the occurrence of global buckling, the lateral deformation also increases. When local buckling occurs, the component can continue to bear load without completely losing its bearing capacity, indicating that the local postbuckling strength of the plate can be utilized. As the local bulge of the plate becomes larger, the lateral bending deformation of the component becomes increasingly obvious, and the specimen is unable to bear more load, reaching the ultimate bearing capacity. When the plate has a relatively small width and thickness and a large length (such as the specimen LC10), the global buckling deformation is obvious, which leads to the global buckling phenomenon. When the plate has a relatively small length and a large width and thickness (such as the specimen LC1), the local buckling phenomenon occurs at the end.

4.1. Ultimate Bearing Capacity. The ultimate bearing capacity of the test specimens is shown in Table 4. It can be found that with the increase in the length of the column, the decreasing rate of ultimate bearing capacity for square

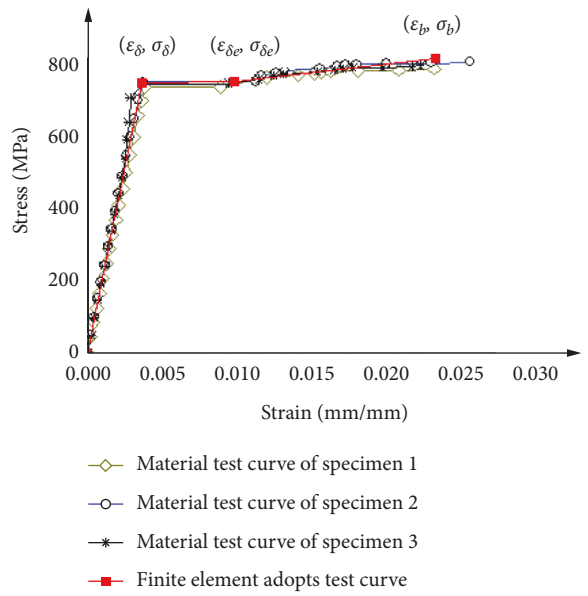

Figure 5: Nominal stress-strain curve of the material.

Figure 6: Snapshots of a member failure.

Table 4: Buckling test results of BS700 HSS groove butt welding box-section members.

Specimen	Length L_0 (mm)	Calculated length L (mm)	Width-thickness ratio (B/t)	Height-thickness ratio (H/t)	Bearing capacity P_{ut} (kN)
LC1	996.3	1156.3	35.5	35.7	700.9
LC2	1398.4	1558.4	35.0	35.0	692.1
LC3	1798.5	1958.5	36.1	35.2	672.6
LC4	2198.2	2358.2	33.0	33.0	609.8
LC5	2600.5	2760.5	32.5	32.9	490.2
LC6	1097.5	1257.5	25.9	36.2	612.1
LC7	1398.6	1558.6	24.6	34.2	604.1
LC8	1597.4	1757.4	24.1	33.4	483.2
LC9	2199.7	2359.7	23.9	33.4	367.2
LC10	2796.6	2956.6	23.3	32.7	238.6

section columns (LC1-LC5) is smaller than that for rectangular section columns (LC6-LC10). This is because the slenderness ratio of weak axis becomes smaller for rectangular section when the height-thickness ratio remains unchanged while the width-thickness ratio decreases. The slenderness ratio has a significant influence on the ultimate bearing capacity of the column when it is large, such as LC4 versus LC9. Meanwhile the width-thickness ratio has a significant influence when the slenderness ratio is smaller, such as LC2 versus LC7.

5. Numerical Simulation Based on Finite Element Method

5.1. Finite Element Model. Numerical analysis is an important method to study the local and global interactive buckling of components. In this paper, ANSYS software is used for the relevant numerical calculation. The parametric model is established to simulate a large number of members with different section sizes and bar lengths.

First, the basic finite element model is established. The unit type shell181 is used to introduce local geometric imperfection and residual stresses. For simplicity, the cold bending effects of the section and chamfering are not considered in the model. To ensure that the member is loaded at the load axis, two rigid plates (which have a large modulus of elasticity) are added to both ends of the member. When the constraint is applied, the node at the center of the plate on both ends can be restrained. Here, a simply supported constraint is adopted. The multilinear strengthening model proposed according to the material test in Figure 5 is adopted, and the basic finite element model is established, as shown in Figure 7.

Next, the geometric imperfection and residual stress are introduced in the established finite element model. Two types of initial defects are considered: local defects and global defects. Local defects are introduced by eigenvalue buckling analysis, and then, the local buckling modes are obtained (as shown in Figure 8), which are multiplied by a certain factor (the maximum value of local buckling deformation divided by H/200) and then introduced into the basic model. Subsequently, for introducing the global defects, the node position of the model is shifted according to the sinusoidal half-wave form, where the maximum defect is δ/L in Table 2, and then, the finite element model is reconstructed according to the migrated node.

For residual stress, the distribution model presented in Figure 9 is adopted based on the existing studies [32].

Here, σ_{ft} represents the residual tensile stress at the weld position of the flange, σ_{fc} represents the residual compressive stress at the flange, σ_{fwt} represents the residual tensile stress at the cold corner, and σ_{wc} represents the residual compressive stress of the web. a_1, b_1, c, a_2, b_2, d_1, e_1, g, e_2, and d_2 represent the length of each distribution area of residual stress. σ_{ft} = (0.7–0.85) f_y, σ_{fwt} = (0.05–0.15) f_y, $\sigma_{fc} = -(0.1–0.25)\ f_y$, $\sigma_{wc} = -(0.1–0.2)\ f_y$, $a_1 = t–2t$, $b_1 = 0.05\ b$, and $d_1 = t–2t$.

$$\begin{aligned} \iint \sigma_r dA &= 0 \\ a_1 + b_1 + c + b_2 + a_2 &= 0.5b \\ a_1 + b_1 + c + b_2 + a_2 &= 0.5b, \end{aligned} \tag{2}$$

where σ_r is the residual stress, b is the width of the section, h is the height of the section, and t is the thickness of the section.

The initial stress data file is preedited, and the element numbering and local coordinates are tracked for the accurate incorporation of initial stress. The initial stress data file is formed through the residual stress model and the mesh gridding of the finite element model. The residual stress is applied at the integral points of elements, where 5 integral points per shell181 element are used.

The entire finite element model mainly consists of five modules: basic analysis module, geometric imperfection introduction module, residual stress introduction module, solution module, and postprocessing module. All the program modules are in a parameterized language to facilitate changing the model according to specific needs. Based on the elastic-plastic theory of large deflection of thin plate, the load-displacement curve of the component is determined by the arc-length method, and the ultimate bearing capacity is obtained.

Figure 7: Basic finite element model.

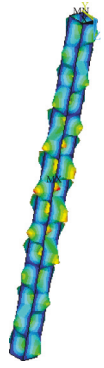

Figure 8: Local buckling modes of components.

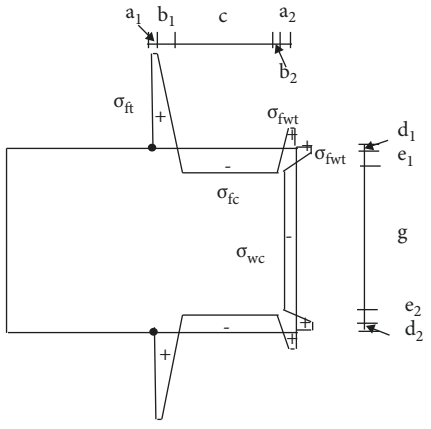

Figure 9: Residual stress model.

5.2. Numerical Simulation Results. A comparison between the finite element simulation results and the experimental

Table 5: Comparison between the test results and finite element simulation results of local and global interactive buckling.

Specimen	λ_x	λ_y	λ_{ny}	P_{us} (kN)	P_{ut} (kN)	$(P_{us}-P_{ut})/P_{ut}$ (%)	P_y (kN)	P_{ut}/P_y
LC1	27.42	27.5	0.5318	715.5	700.9	2.08	917.8	0.7637
LC2	37.13	37.16	0.7187	682.2	692.1	−1.43	926.6	0.7469
LC3	47.22	46.33	0.8961	695.2	672.6	3.36	906.5	0.7420
LC4	55.98	56.10	1.0851	581.6	609.8	−4.62	990.9	0.6154
LC5	65.55	66.12	1.2791	474.6	490.2	−3.18	993.5	0.4934
LC6	31.33	40.64	0.7862	621.2	612.1	1.49	765.1	0.8000
LC7	38.98	50.44	0.9756	592.3	604.1	−1.95	804.7	0.7507
LC8	44.44	57.39	1.1101	459.8	483.2	−4.84	806.8	0.5989
LC9	58.94	76.6	1.4817	352.6	367.2	−3.98	825.3	0.4449
LC10	73.67	96.15	1.8599	225.2	238.6	−5.62	846.9	0.2817

results is presented in Table 5. Here, P_y represents the bearing capacity of the section at full yield: $P_y = Af_y$; P_{ut} represents the buckling capacity measured in the test; λ_x is the slenderness ratio of the specimen around the strong axis; λ_y is the slenderness ratio of the specimen around the weak axis; λ_{ny} is the regularized slenderness ratio, which is calculated according to the Chinese specification [23] using the following equation:

$$\lambda_{ny} = \frac{\lambda_y}{\pi}\sqrt{\frac{f_y}{E}}. \tag{3}$$

Here, P_{us} is the simulated bearing capacity from the finite element analysis, P_{ut} is the test carrying capacity, and P_y is the full section yield strength.

It is clear from Table 5 that except for some components (LC10), the difference between the ultimate bearing capacity of the specimens obtained by experiment and finite element simulation is within 5%, and most of the simulation results are lower than the experimental values, indicating that the established finite element analysis model is reasonable and feasible, and the results are also conservative. To further compare the finite simulation and test results, the load-displacement curves obtained by the two methods are shown in Figure 10.

It is clear from the load-axial displacement curve and load-lateral displacement curve of each specimen in Figure 10 that the specimens mainly exhibit local and global interactive buckling failure. Taking LC4 as an example, when the load is small, the specimen is in an elastic state. The load-axial displacement curves in Figure 10(a) are approximately linear and their slope remains basically the same, while the load-lateral displacement curves in Figure 10(c) show a slight change. As the load increases, buckling occurs near the central position of the first web bar. As the load continues to increase, due to the local buckling of the web, the load-axial displacement curve becomes nonlinear. Further, the lateral displacement of the central node of the specimen also enters the nonlinear stage and increases sharply. The local buckling load continues to increase the buckling of the flange and whole specimen. Furthermore, the specimen reached the load limit. At this time, the lateral displacement of the middle node of the specimen increases horizontally and the axial load is slowly unloaded. When the load decreases to a certain value, the specimen exhibits sudden failure, and the loading is stopped. It may be noted that the descending stage of many specimens could not be obtained through the test. Meanwhile, the local bulge of the plate is not always located in the middle of the bar, so the effective load-lateral displacement curve of some specimens (such as LC2 and LC3) could not be determined. Overall, the simulation curves are in excellent agreement with the test curves. This proves that the proposed finite element model can well simulate the compressive failure process of a thin-walled box-section pressure bar made of BS700 HSS material.

6. Comparison with the Design Codes of Steel Structures

6.1. China Standard Calculation Method. According to the Chinese Design Code for Steel Structures [23], when the width-thickness ratio of the plate exceeds the limit value, considering the postbuckling strength, the stability of the axial compression member is calculated as follows:

$$\frac{N}{\varphi A_c f} \le 1, \tag{4}$$

where $A_c = \sum \rho_i A_i$. A_c is the effective gross cross-sectional area, Ai is the gross cross-sectional area of each panel, φ is the stability factor calculated by gross cross section, and ρ_i is the effective cross-section factor of each plate.

According to equation (7), if the local buckling is taken into account, the global and local interactive stability factor of the component should be reduced based on the gross cross-section stability factor. This factor is defined as follows:

$$\varphi_z = \frac{\Sigma \rho_i A_i}{\Sigma A_i}. \tag{5}$$

The effective cross-section factor of the plate ρ_i is specified as follows:$\lambda \le 40\sqrt{235/f_y}$. When the yield strength is 700 MPa, $\lambda \le 23.18$, so

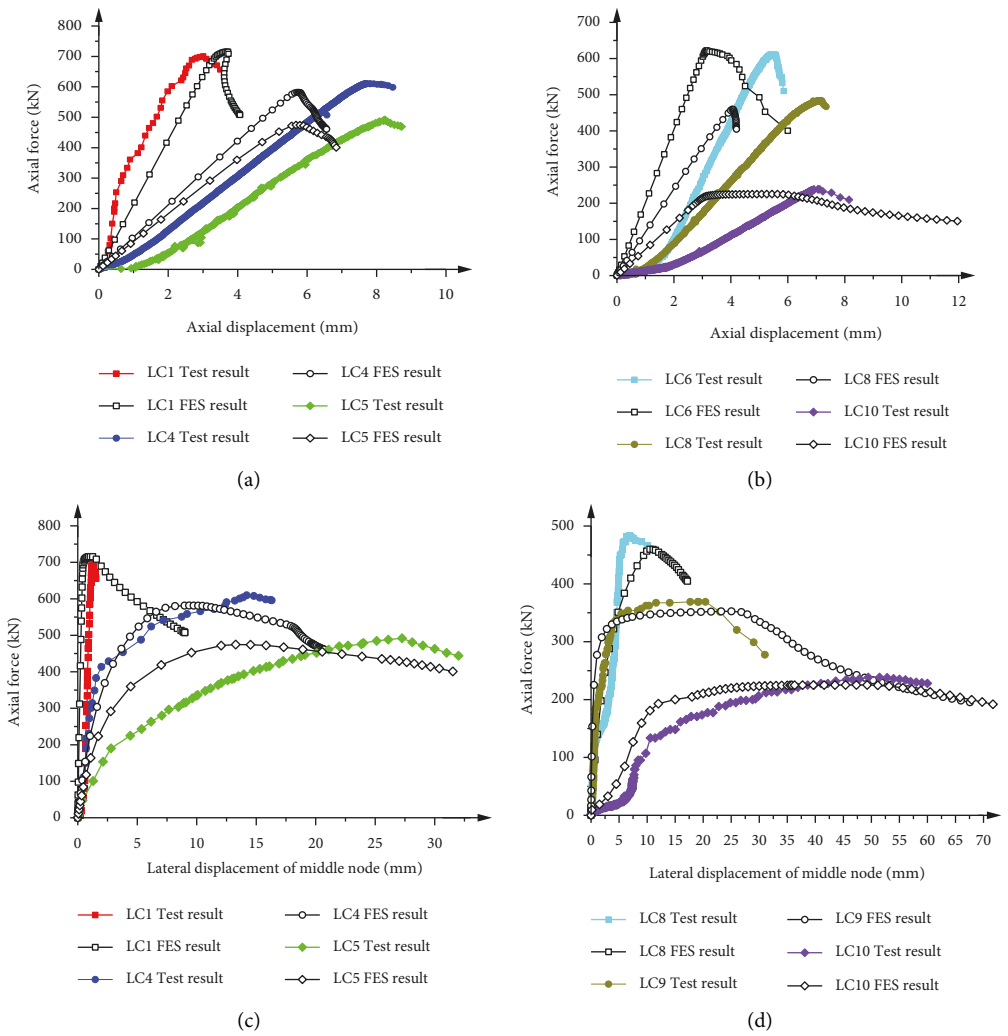

FIGURE 10: Comparison between the load-displacement curves obtained by experimental test and finite element simulation. (a) Load-axial displacement curves of specimens 1, 4, and 5. (b) Load-axial displacement curves of specimens 6, 8, and 10. (c) Load-lateral displacement curves of specimens 1, 4, and 5. (d) Load-lateral displacement curves of specimens 8, 9, and 10.

$$\rho = 1, \tag{6}$$

$\lambda > 52\sqrt{235/f_y}$. When the yield strength is 700 MPa, $\lambda > 30.13$, so

$$\rho \geq \left(29\sqrt{\frac{235}{f_y}} + 0.25\lambda\right)\frac{t}{b}. \tag{7}$$

Here, b is the width of the plate, and t is the thickness of the plate.

$$\begin{aligned} &\rho \geq (16.8 + 0.25\lambda)\frac{t}{b}, \\ &\frac{b}{t} > 42\sqrt{\frac{235}{f_y}}, \frac{b}{t} > 24.34, \\ &\rho = \frac{1}{\lambda_{n,p}}\left(1 - \frac{0.19}{\lambda_{n,p}}\right). \end{aligned} \tag{8}$$

Here, $\lambda_{n,p} = b/t/56.2\sqrt{235/f_y}$; i.e., $\lambda_{n,p} = b/t/32.56$.

6.2. US Standard Calculation Method. According to the American ANSI/AISC 360–10 specification [15], the bearing capacity of axial compression members is calculated as follows:

$$P_n = F_{cr}A_g, \tag{9}$$

where P_n represents the nominal compressive strength, A_g is the gross cross-sectional area, F_{cr} is the flexural buckling stress, and the factor Q is introduced to consider the influence of local buckling of plate parts. The calculation formula is as follows:

$$\frac{KL}{r} \leq 4.71\sqrt{\frac{E}{Qf_y}}, \tag{10}$$

$$\frac{KL}{r} > 4.71\sqrt{\frac{E}{Qf_y}}, \tag{11}$$

where $F_e = \pi^2 E/(KL/r)^2$ is the critical elastic buckling stress, K is the calculated length factor of the member, L is the length of

the member, r is the rotational radius of the section of the member, so it is actually the slenderness ratio, and Q is the reduction factor after considering the local buckling of the plate.

The stability factor is defined as $\varphi = P_n/P_y$. Substituting it in equation (12) and using $P_y = f_y A_g$, we get

$$\varphi = \frac{F_{\mathrm{cr}}}{\mathrm{f}_y}. \tag{12}$$

The slenderness ratio can be normalized to obtain the regularized fineness ratio as follows:

$$\lambda_n = \frac{\lambda}{\pi}\sqrt{\frac{f_y}{E}}. \tag{13}$$

Substituting equations (13), (14), and (16) into equation (15), it can be obtained that

$$\begin{aligned} \lambda_{\mathrm{n}} &\le \frac{1.4992}{\sqrt{Q}} \\ \lambda_n &> \frac{1.4992}{\sqrt{Q}}, \varphi = \frac{0.877}{\lambda_n^2}. \end{aligned} \tag{14}$$

According to the different width-thickness ratios of the pressed plate, the sections can be divided into three types: compact section, noncompact section, and flexible section. The first two sections do not consider the influence of local buckling of the plate; i.e., $Q = 1$. The impact of plate buckling needs to be considered in the flexible section, and the relevant stability design is necessary; i.e., $Q = QsQa$. For the box section, $Qs = 1$.

$$Q = \mathrm{Q}_a = \frac{A_{\mathrm{eff}}}{A_g}. \tag{15}$$

It can be seen from equation (19) that the factor Q is related to the effective cross-sectional area $\mathrm{A_{eff}}$, and the effective width of the panel is required. For elements under uniform compression (except box-section flange), the effective height of the box-section web when $h/t \ge 1.49\sqrt{E/f}$ can be obtained as follows:

$$h_e = 1.92t\sqrt{\frac{E}{f}}\left(1 - \frac{0.34}{\mathrm{h/t}}\sqrt{\frac{E}{f}}\right) \le h, \tag{16}$$

where $f = F_{cr}$, and F_{cr} is calculated by considering $Q = 1$ in equations (13) and (14).

When $b/t \ge 1.4\sqrt{E/f}$, the effective width of the box-section flange is

$$b_e = 1.92t\sqrt{\frac{E}{f}}\left(1 - \frac{0.38}{\mathrm{b/t}}\sqrt{\frac{E}{f}}\right) \le b, \tag{17}$$

where $f = P_{\mathrm{n}}/A_{\mathrm{eff}}$. For convenience, it is considered that $f = f_y$.

6.3. European Standard Calculation Method. In the European design specification for steel structures (BS EN 1993-1-1 Eurocode 3 [22]), according to the effect of local buckling of the plate on the bearing performance, the cross section is divided into four types. In the former three kinds of cross sections, the effect of local buckling is not considered in the design process. For the fourth kind of cross section, the buckling capacity can be calculated using the effective cross-sectional area as follows:

$$N_{b,R\,d} = \frac{\chi A_{\mathrm{eff}} f_y}{\gamma_{M1}}, \tag{18}$$

where $N_{b,Rd}$ is the buckling capacity, A_{eff} is the cross-sectional area of the plate after the local buckling, f_{y} is the yield strength of the material, and γ_{M1} is the partial factor of the material, which is equal to 1 in this study. χ is the corresponding buckling stability factor. It is calculated as follows:

$$\chi = \frac{1}{\varphi + \sqrt{\varphi^2 - \overline{\lambda}^2}} \text{ and } x \le 1, \tag{19}$$

where

$$\varphi = 0.5\left[1 + \alpha(\overline{\lambda} - 0.2) + \overline{\lambda}^2\right]. \tag{20}$$

Here, $\overline{\lambda}$ is the regularized slenderness ratio, and the effective area A_{eff} is used for reduction, i.e., $\overline{\lambda} = \sqrt{A_{\mathrm{eff}} f_y / N_{\mathrm{cr}}}$, where N_{cr} is the critical elastic stable force of the gross cross section without considering the local buckling of the plate, and it can be obtained that

$$\overline{\lambda} = \sqrt{\frac{A_{\mathrm{eff}} f_y}{N_{cr}}} = \frac{\lambda}{\pi}\sqrt{\frac{f_y}{E}}\sqrt{\frac{A_{\mathrm{eff}}}{A}}. \tag{21}$$

α is the defect influence factor. Each kind of column curve corresponds to one kind of defect influence factor, and five column curves are specified. The welded box section belongs to the column curve of Class C when the width-thickness ratio is less than 30 and Class B when it is greater than or equal to 30. For Class B, $\alpha = 0.34$, and for Class C, $\alpha = 0.49$.

According to the definition of stability factor,

$$\varphi = \frac{N_{b,\mathrm{Rd}}}{\mathrm{N_y}} = \frac{\chi A_{\mathrm{eff}} f_y}{\gamma_{M1} A f_y} = \chi\frac{A_{\mathrm{eff}}}{A}. \tag{22}$$

The effective area A_{eff} is calculated as follows:

$$A_{\mathrm{eff}} = \rho A, \tag{23}$$

where ρ is the reduction factor associated with the type of plate. For a two-sided supported plate,

$$\begin{aligned} \rho &= 1, \overline{\lambda_p} \le 0.673 \\ \rho &= \frac{\overline{\lambda_p} - 0.055(3 + \psi)}{\overline{\lambda_p}^2} - \le 1, \overline{\lambda_p} > 0.673 \end{aligned} \tag{24}$$

where $\overline{\lambda_p}$ is the regularized width-thickness ratio, which is calculated as follows:

$$\overline{\lambda_p} = \frac{b/t}{28.4\sqrt{k_a}}\sqrt{\frac{f_y}{235}}. \tag{25}$$

Table 6: Comparison between the test results and the results obtained by Chinese, US, and European codes.

Specimen	φ_f	φ_c	$(\varphi_f-\varphi_c)/\varphi_f$ %	φ_a	$(\varphi_f-\varphi_a)/\varphi_f$ %	φ_e	$(\varphi_f-\varphi_e)/\varphi_f$ %
LC1	0.7637	0.6486	15.1	0.6967	8.8	0.6647	13.0
LC2	0.7469	0.5885	21.2	0.6652	10.9	0.6158	17.6
LC3	0.7420	0.5013	32.4	0.6095	17.9	0.5461	26.4
LC4	0.6154	0.4389	28.7	0.5677	7.8	0.4848	21.2
LC5	0.4934	0.3559	27.9	0.4852	1.7	0.4034	18.2
LC6	0.8000	0.6122	23.5	0.6946	13.2	0.6304	21.2
LC7	0.7507	0.5367	28.5	0.6439	14.2	0.5581	25.7
LC8	0.5989	0.4707	21.4	0.5878	1.9	0.4940	17.5
LC9	0.4449	0.3111	30.1	0.3973	10.7	0.3360	24.5
LC10	0.2817	0.2138	24.1	0.2524	10.4	0.2326	17.4
Average error	25.29		9.75		20.27		

ψ is the stress distribution ratio of the the compression member plate. For the axial compression member, $\psi = 1$, and k_a is a factor associated with factor ψ. For a bilateral support plate, when $\psi = 1$, $k_a = 4$. According to the specific values of ψ and k_a, (24) and (25) can be rewritten as

$$\begin{aligned} &\rho = 1, \overline{\lambda_p} \le 0.673 \\ &\rho = \frac{\overline{\lambda_p} - 0.22}{\overline{\lambda_p}^2} \le 1, \\ &\overline{\lambda_p} > 0.673, \\ &\overline{\lambda_p} = \frac{b/t}{56.8}\sqrt{\frac{f_y}{235}}. \end{aligned} \tag{26}$$

6.4. Comparison between the Experimental Results and the Standard Results of Different Countries. The stability factors calculated by national codes are compared with the test results in Table 6.

Here, φ_f is the test stability factor. φ_c, φ_a, and φ_e are the stability factors corresponding to the Chinese, US, and European codes, respectively. It can be seen from Table 6 that the average error between the test and the Chinese code results is 25.29% and the standard deviation is 5.19%. For the US code, these values are 9.75% and 5.07%, respectively. For the European code, these values are 20.27% and 4.31%, respectively. The US code data is close to the test result, while the Chinese code and the European code appear more conservative. However, the difference between the test results and any national specification data is more than 5%. The main reason for the discrepancy between the test results and different code results is that the effective section calculation method and global buckling stability factor are different. Furthermore, the above results indicate that the existing codes for BS700 HSS thin-walled box-section members are relatively conservative for determining the local and global buckling interactive capacity, which warrants further research to derive a new calculation formula.

7. Conclusions

The local and global interactive buckling capacities of the thin-walled box-section members formed by cold bending of BS700 HSS were experimentally investigated. Further, a finite element model was proposed to simulate the test process. The main results of the study are summarized as follows:

(1) By measuring the initial geometric imperfection of the whole specimen, it was found that the maximum initial deflection was nearly 1/1000 of the length of the bar. Thus, the initial deflection during design could be determined according to 1/1000 of the length of the bar as stipulated in the existing code of China.

(2) Based on the material performance test of BS700 HSS, it was found that the material had a certain yield platform and good plastic performance. The ratio of yield strength to tensile strength was 0.9340, which was higher than that of ordinary low-strength steel.

(3) The local and global interactive buckling tests of 10 BS700 HSS thin-walled box-section axial compression members were conducted, and the failure modes were found to be local and global interactive buckling failures.

(4) The residual stress and geometric imperfection of thin-walled box-section members of BS700 HSS were introduced in the finite element model to obtain the local and global interactive buckling capacity. It was proved that the established finite element model could effectively simulate the local and global buckling failure process of the specimens under axial compression. The model provided nearly accurate ultimate bearing capacity, which proved its efficacy and feasibility.

(5) The ultimate bearing capacities of the tested members were higher than the values obtained by the steel structure design codes of China, the USA, and Europe. The Chinese code and the European code were found to be more conservative with a difference of more than 20%. The US specification data were closer to the test results, but they were also smaller

than the test values by nearly 10%. This indicates that the existing codes are relatively conservative for calculating the local and global interactive buckling capacity of the thin-walled box-section members of BS700 HSS under axial compression, and further research is needed.

Data Availability

The data used to support the findings of this study are included within the article.

Conflicts of Interest

The authors declare that they have no conflicts of interest or personal relationships that could have appeared to influence the work reported in this paper.

Authors' Contributions

Gao Lei contributed to the methodology and writing the original draft; Ni ming, investigation, writing the original draft, reviewing and editing, and visualization; Xie Xingkun, conceptualization, validation, formal analysis, methodology, and reviewing and editing; Bai Linyue, methodology, investigation, and reviewing and editing; He Lixiang, conceptualization, validation, and writing the original draft.

Acknowledgments

This research was funded by the Project of the Major State Basic Development of China (973 program, grant number: 2014CB046801).

References

[1] Y. Ding, D. Wu, J. Su, Z.-X. Li, L. Zong, and K. Feng, "Experimental and numerical investigations on seismic performance of RC bridge piers considering buckling and low-cycle fatigue of high-strength steel bars," *Engineering Structures*, vol. 227, Article ID 111464, 2021.

[2] O. Skoglund, J. Leander, and R. Karoumi, "Optimizing the steel girders in a high strength steel composite bridge," *Engineering Structures*, vol. 221, Article ID 110981, 2020.

[3] E. Cadoni and D. Forni, "Strain-rate effects on S690QL high strength steel under tensile loading," *Journal of Constructional Steel Research*, vol. 175, Article ID 106348, 2020.

[4] L. Qiu, Y. Liu, Z. Hou, S. Chen, and K. Chung, "State application research of high strength steel in steel structures," *Industrial Construction*, vol. 44, no. 3, pp. 1–5, 2014.

[5] G. Pocock, "High strength steel use in Australia, Japan and the US," *Structural Engineer*, vol. 84, pp. 27–30, 2006.

[6] A.-M. Arola, A. Kaijalainen, V. Kesti, L. Troive, J. Larkiola, and D. Porter, "The effect of mechanical behavior on bendability of ultrahigh-strength steel," *Materials Today Communications*, vol. 26, Article ID 101943, 2021.

[7] J. Wang, S. Afshan, and L. Gardner, "Axial behaviour of prestressed high strength steel tubular members," *Journal of Constructional Steel Research*, vol. 133, pp. 547–563, 2017.

[8] H. P. Günther, *Use and Application of High-Performance Steels for Steel Structures*, ETH Honggerberg, Zurich, Switzerland, 2006.

[9] H. Shen and H. Ren, "Recent advances in research on stability behavior of high strength steel members," *Progress in Steel Building Structures*, vol. 19, pp. 53–62, 2017.

[10] B. He, *Research on Fire Resistance Performance of Rec-Section Q550 High-Strength Steel Column with Axial Compression*, Southeast university, Nanjing, china, 2018.

[11] Y. Xu, *Research on Bucking Behavior of 800 Mpa High-Strength Steel Welded I-Section Member under Axial Compression*, Anhui University of Technology, Hefei, china, 2018.

[12] L. Gao, H. Sun, and G. Xu, "Stability study on thin-walled box-section beam of high strength steel," *Building Structure*, vol. 40, pp. 12–15, 2010.

[13] L. Gao, K. Jiang, L. Bai, and Q. Wang, "Experimental study on stability of high strength steel long columns with box-sections," *Advanced Steel Construction*, vol. 13, pp. 399–411, 2017.

[14] G. H. Little, "The strength of square steel box columns-design curves and their theoretical-basis," *Structural Engineer*, vol. 57A, no. 2, pp. 49–61, 1979.

[15] Ansi/Aisc 360-10, *Specification for Structural Steel Buildings*, American Institute of Steel Construction, Chicago, USA, 2010.

[16] H. Amouzegar, B. W. Schafer, and M. Tootkaboni, "An incremental numerical method for calculation of residual stresses and strains in cold-formed steel members," *Thin-Walled Structures*, vol. 106, pp. 61–74, 2016.

[17] B. W. Schafer, "Review: the Direct Strength Method of cold-formed steel member design," *Journal of Constructional Steel Research*, vol. 64, no. 7, pp. 766–778, 2008.

[18] G. J. Hancock, "Nonlinear analysis of thin sections in compression," *Journal of the Structural Division*, vol. 107, no. 3, pp. 455–471, 1981.

[19] T. Usami and Y. Fukumoto, "Local and overall buckling of welded box columns," *Journal of the Structural Division*, vol. 108, no. 3, pp. 525–542, 1982.

[20] T. Usami and Y. Fukumoto, "Welded box compression members," *Journal of Structural Engineering-asce - J STRUCT ENG-ASCE*, vol. 110, 1984.

[21] W. W. Yu, *Cold-formed Steel Design*, Water Power Press, Beijing, China, 2003.

[22] Bs En 1993-1-1 Eurocode 3, *Design of Steel Structures, Part 1-1: General Rules and Rules for Buildings*, European Committee for Standardization, Brussels, 2005.

[23] Gb50017-2017, *Code for Design of Steel Structures*, China Building Industry Press, Beijing, China, 2017.

[24] N. E. Shanmugam, J. Y. R. Liew, and S. Lee, "Thin-walled steel box columns under biaxial loading," *Journal of Structural Engineering-asce - J STRUCT ENG-ASCE*, vol. 115, 1989.

[25] H. Degée, A. Detzel, and U. Kuhlmann, "Interaction of global and local buckling in welded RHS compression members," *Journal of Constructional Steel Research*, vol. 64, no. 7, pp. 755–765, 2008.

[26] Z. Lin Xiong, *Interaction of global and local buckling in thin-wall welded rectangular hollow section compression members*, Xi'an University of Architecture and Technology, Xi'an, china, 2010.

[27] H. X. Shen, "Local-overall interaction buckling of high strength steel welded square box columns," *Gongcheng Lixue/Engineering Mechanics*, vol. 29, pp. 221–227, 2012.

[28] S. F. Chen, "Stub-column test and interactive local-global buckling of steel compression," *Progress in Steel Building Structures*, vol. 15, no. 02, pp. 1–5, 2013.

[29] G. Shu, Z. Shi, and Z. Li, "Experimental study on local stability and correlation stability of Q550 high-strength steel welded box section members under axial compression," *Steel Construction*, vol. 31, no. 2, pp. 10–17, 2016.

[30] X. Liu, "Bucking FEM modeling and verification for high-strength steel box section components under axial and eccentric compressions," *Building Structure*, vol. 47, no. 15, pp. 49–53, 2017.

[31] Gb/T 2975-2018, *Steel and Steel Products—Location and Preparation of Samples and Test Pieces for Mechanical Testing*, China Standard Press, Beijing, China, 2018.

[32] X. Xie, F. Shao, L. Gao, L. He, and L. Bai, "Research on residual stress of a BS700 butt-welded box section and its influence on the stability of axial compression members," *Materials*, vol. 13, no. 15, p. 3282, 2020.